

# Achievable Efficiency of Numerical Methods for Simulations of Solar Surface Convection

H. Grimm-Strele<sup>a,1,\*</sup>, F. Kupka<sup>a</sup>, H. J. Muthsam<sup>a</sup>

<sup>a</sup>*Institute of Mathematics, University of Vienna, Oskar-Morgenstern-Platz 1, A-1090 Vienna, Austria*

## Abstract

We investigate the achievable efficiency of both the time and the space discretisation methods used in Antares for mixed parabolic–hyperbolic problems. We show that the fifth order variant of WENO combined with a second order Runge–Kutta scheme is not only more accurate than standard first and second order schemes, but also more efficient taking the computation time into account. Then, we calculate the error decay rates of WENO with several explicit Runge–Kutta schemes for advective and diffusive problems with smooth and non-smooth initial conditions. With this data, we estimate the computational costs of three-dimensional simulations of stellar surface convection and show that SSP RK(3,2) is the most efficient scheme considered in this comparison.

**Keywords:** Methods: numerical, Numerical astrophysics, Runge–Kutta schemes, efficiency, WENO scheme, Hydrodynamics

The simulation code Antares [1] was developed for the simulation of solar and stellar surface convection. Recently it has also been applied to many other astrophysical problems [e.g. 2, 3].

In this code, the Navier–Stokes equations (usually without magnetic field) and with radiative transfer (radiation hydrodynamics, RHD) are solved in the form

$$\frac{\partial \rho}{\partial t} + \nabla \cdot (\rho \mathbf{u}) = 0, \quad (1a)$$

$$\frac{\partial (\rho \mathbf{u})}{\partial t} + \nabla \cdot (\rho \mathbf{u} \otimes \mathbf{u}) + \nabla p = \rho \mathbf{g} + \nabla \cdot \tau, \quad (1b)$$

$$\frac{\partial E}{\partial t} + \nabla \cdot (\mathbf{u} (E + p)) = \rho (\mathbf{g} \cdot \mathbf{u}) + \nabla \cdot (\mathbf{u} \cdot \tau) + Q_{\text{rad}}. \quad (1c)$$

The meaning and units of all variables is shown in Table 1. An equation of state must be specified to complete this set of equations. The viscous stress tensor  $\tau = (\tau_{i,j})_{i=1,2,3}$  is given by

$$\tau_{i,j} = \eta \left( \frac{\partial u_i}{\partial x_j} + \frac{\partial u_j}{\partial x_i} - \frac{2}{3} \delta_{i,j} (\nabla \cdot \mathbf{u}) \right) + \zeta \delta_{i,j} (\nabla \cdot \mathbf{u}). \quad (2)$$

$\mathbf{g}$  is the gravity vector and  $Q_{\text{rad}}$  is the radiative heating rate describing the energy exchange between gas and radiation.  $\delta_{i,j}$  is the Kronecker symbol.  $\eta$  and  $\zeta$  are the first and second coefficients of viscosity.

We can rewrite equations (1) as

$$\frac{\partial \mathbf{Q}}{\partial t} + \nabla \cdot \mathbf{F}_{\text{adv}} = \nabla \cdot \mathbf{F}_{\text{visc}} + \mathbf{S} \quad (3a)$$

variable	meaning	unit (CGS)
$\rho$	gas density	$\text{g cm}^{-3}$
$T$	temperature	K
$p$	pressure	$\text{dyn cm}^{-2}$
$u$	$x$ velocity (vertical)	$\text{cm s}^{-1}$
$v$	$y$ velocity (horizontal)	$\text{cm s}^{-1}$
$w$	$z$ velocity (horizontal)	$\text{cm s}^{-1}$
$Q_{\text{rad}}$	radiative heating rate	$\text{erg s}^{-1} \text{cm}^{-3}$
$v_{\text{snd}}$	sound speed	$\text{cm s}^{-1}$
$E$	total energy	$\text{erg cm}^{-3}$
$e$	internal energy	$\text{erg cm}^{-3}$
$\epsilon$	specific internal energy	$\text{erg g}^{-1}$
$\eta$	dynamic viscosity	$\text{g cm}^{-1} \text{s}^{-1}$
$\zeta$	second (bulk) viscosity	$\text{g cm}^{-1} \text{s}^{-1}$

Table 1: Variable names, meaning and CGS units as used in this paper. Note that  $x$  denotes the vertical direction. Vectors are written in bold face. The velocity vector is  $\mathbf{u} = (u, v, w)^T$ .

with

$$\mathbf{Q} = \begin{pmatrix} \rho \\ \rho \mathbf{u} \\ E \end{pmatrix}, \mathbf{F}_{\text{adv}} = \begin{pmatrix} \rho \mathbf{u} \\ \rho \mathbf{u} \otimes \mathbf{u} + p \text{Id} \\ \mathbf{u} (E + p) \end{pmatrix}, \quad (3b)$$

$$\mathbf{F}_{\text{visc}} = \begin{pmatrix} 0 \\ \tau \\ \mathbf{u} \cdot \tau \end{pmatrix}, \mathbf{S} = \begin{pmatrix} 0 \\ \rho \mathbf{g} \\ \rho (\mathbf{g} \cdot \mathbf{u}) + Q_{\text{rad}} \end{pmatrix}.$$

$\mathbf{Q}$  is the vector containing the conserved quantities and Id is the identity matrix. We call the terms collected in  $\mathbf{F}_{\text{adv}}$  the *advective* or *inertial* part and in  $\mathbf{F}_{\text{visc}}$  the *viscous* part of the Navier–Stokes equations. All first derivatives are contained in  $\nabla \cdot \mathbf{F}_{\text{adv}}$ , all second order terms in  $\nabla \cdot \mathbf{F}_{\text{visc}}$ . We note that  $\frac{\partial \mathbf{Q}}{\partial t} + \nabla \cdot \mathbf{F}_{\text{adv}} = 0$  is of hyperbolic type, whereas  $\frac{\partial \mathbf{Q}}{\partial t} - \nabla \cdot \mathbf{F}_{\text{visc}} = 0$  is a parabolic system.

\*corresponding author

Email address: hannes.grimm-strele@univie.ac.at  
(H. Grimm-Strele)

<sup>1</sup>Present address: Max–Planck Institute for Astrophysics, Karl–Schwarzschild–Strasse 1, D-85748 Garching, Germany

## 1. Discretisation and Numerical Methods

Following the *method of lines* approach of discretising space and time separately [4, 5], equations (3) are discretised in space only and converted to

$$\frac{\partial \mathbf{Q}}{\partial t} = \mathbf{L}(\mathbf{Q}), \quad (4)$$

where  $\mathbf{L}$  is the operator resulting from the spatial discretisation of  $-\nabla \cdot \mathbf{F}_{\text{adv}} + \nabla \cdot \mathbf{F}_{\text{visc}} + \mathbf{S}$ . In principle, the integration of this equation can be performed with any numerical method for solving ordinary differential equations, in particular Runge–Kutta methods, provided they are numerically stable, although further properties (such as positivity, e.g., of  $T$  or  $E$ ) may be required (cf., for instance, Kupka et al. [6]).

The spatial discretisation is done separately for  $\mathbf{F}_{\text{adv}}$  and  $\mathbf{F}_{\text{visc}}$  as defined in equations (3). In optically thin regions the radiative heating rate  $Q_{\text{rad}}$  is a source term and is calculated separately by the radiative transfer solver as described in Muthsam et al. [1]. In optically thick regions, the diffusion approximation

$$Q_{\text{rad}} = \nabla \cdot (\kappa \nabla T) \quad (5)$$

is valid such that we can include  $Q_{\text{rad}}$  in the  $\mathbf{F}_{\text{visc}}$  term.

For  $\mathbf{F}_{\text{adv}}$ , the WENO finite difference scheme is employed [7, 8, 9]. The WENO scheme is a highly efficient shock-capturing scheme which we consider here in its fifth order variant called WENO5. In the context of solar surface convection simulations, its superiority in terms of accuracy compared to other high-order schemes was shown in Muthsam et al. [10]. Its main part, the fifth order accurate reconstruction operator, is summarised in Algorithm 3.

For  $\mathbf{F}_{\text{visc}}$ , the fourth-order accurate scheme from Happenhofer et al. [11] is used. First, we outline the procedure for the one-dimensional diffusion equation

$$\frac{\partial \phi}{\partial t} - D \frac{\partial^2 \phi}{\partial x^2} = \frac{\partial \phi}{\partial t} - \frac{\partial}{\partial x} \left( D \frac{\partial \phi}{\partial x} \right) = 0 \quad (6)$$

with the constant coefficient of diffusion  $D$ . In one spatial dimension and on an equidistant Cartesian grid, the outer derivative is approximated by

$$\frac{\partial}{\partial x} \left( \frac{\partial \phi}{\partial x} \right) (x_i) = \frac{\frac{\partial \phi}{\partial x} (x_{i+\frac{1}{2}}) - \frac{\partial \phi}{\partial x} (x_{i-\frac{1}{2}})}{\delta x} \quad (7a)$$

with constant grid spacing  $\delta x$ . Then, the inner derivative is calculated by

$$\frac{\partial \phi}{\partial x} (x_{i-\frac{1}{2}}) = \frac{\phi_{i-2} - 15\phi_{i-1} + 15\phi_i - \phi_{i+1}}{12 \delta x}, \quad (7b)$$

leading to a fourth-order accurate approximation. Here,  $\phi_i = \phi(x_i)$ .

Similar procedures can be applied to any second-order term, in particular to  $\mathbf{F}_{\text{visc}}$ . Special care has to be taken for mixed derivatives. In the two-dimensional case and considering only the  $\mathbf{F}_{\text{visc}}$  terms, we arrive at

$$\frac{\partial}{\partial t} (\rho u) = \frac{\partial}{\partial x} \left( \left( \zeta + \frac{4}{3} \eta \right) \frac{\partial u}{\partial x} + \left( \zeta - \frac{2}{3} \eta \right) \frac{\partial v}{\partial y} \right) + \frac{\partial}{\partial y} \left( \eta \left( \frac{\partial u}{\partial x} + \frac{\partial v}{\partial y} \right) \right) \quad (8)$$

by virtue of equations (1) and (2). The outer derivatives are replaced by a finite difference, evaluating the inner function at the half-integer nodes. Therefore, we need the terms inside the spatial derivatives in (8) at  $(i-\frac{1}{2}, j)$  and at  $(i, j-\frac{1}{2})$ .  $\frac{\partial u}{\partial x}$  at  $(i-\frac{1}{2}, j)$  and  $\frac{\partial v}{\partial y}$  at  $(i, j-\frac{1}{2})$  can be calculated directly by formula (7b). Then, the coefficient functions must be interpolated to the half-integer grid. To fourth-order accuracy,

$$\eta_{i-\frac{1}{2},j} = \frac{-\eta_{i-2,j} + 7\eta_{i-1,j} + 7\eta_{i,j} - \eta_{i+1,j}}{12}, \quad (9)$$

assuming that the variable is given as a cell average. To calculate  $\frac{\partial v}{\partial y}$  at the half integer index  $(i-\frac{1}{2}, j)$ , we calculate the derivative at the cell centre by

$$\frac{\partial v}{\partial y}|_{i,j} = \frac{v_{i,j-2} - 8v_{i,j-1} + 8v_{i,j+1} - v_{i,j+2}}{12 \delta y}, \quad (10)$$

and then interpolate the result to  $(i-\frac{1}{2}, j)$  according to formula (9). The computation of  $\frac{\partial u}{\partial x}$  at  $(i, j-\frac{1}{2})$  is done analogously. The resulting procedure is fourth-order accurate.

After the spatial discretisation step, the equations (1) are transformed to the form (4). Since (4) is an ordinary differential equation, we can use Runge–Kutta schemes to integrate it.

We follow Gottlieb et al. [12] in defining some basic properties of Runge–Kutta schemes.

**Definition 1.** Let an initial value problem of the form

$$\phi'(t) = \mathbf{L}(\phi(t)), \quad \phi(0) = \phi_0, \quad (11)$$

be given. An explicit  $s$ -stage Runge–Kutta scheme is an integration scheme of the form

$$\begin{aligned} \phi^{(0)} &= \phi^n, \\ \phi^{(i)} &= \sum_{k=0}^{i-1} (\alpha_{i,k} \phi^{(k)} + \delta t \beta_{i,k} \mathbf{L}(\phi^{(k)})), \quad \alpha_{i,k} \geq 0, \quad i = 1, \dots, s, \\ \phi^{n+1} &= \phi^{(s)}, \end{aligned} \quad (12)$$

where  $\phi^n = \phi(t_n)$  and the time step  $\delta t$  is given by the CFL condition.

**Definition 2.** Assume that  $\mathbf{L}$  results from the discretisation of a spatial operator and let a seminorm  $\|\cdot\|$  be given. Following Wang and Spiteri [13], a Runge–Kutta method of the form (12) is called strong stability preserving (SSP) if for all stages  $i$ ,  $i = 1, 2, \dots, s$ ,

$$\|\phi^{(i)}\| \leq \|\phi^n\| \quad (13)$$

with a CFL restriction on the time step  $\delta t$ .

The *total variation diminishing (TVD)* property [7] is a special case of this definition. It results from inserting the *total variation* norm of  $\phi$  at time  $t_n$ ,

$$\text{TV}(\phi^n) = \sum_j |\phi_{j+1}^n - \phi_j^n|, \quad (14)$$

in (13).

In this paper, we consider four explicit time integration schemes: the first-order Euler forward method, the second-order two-stage TVD2 and the third-order three-stage TVD3 scheme from Shu and Osher [7]. The fourth explicit scheme is the second-order three-stage scheme from Kraaijevanger [14], further studied in Ketcheson et al. [15] and Kupka et al. [6], called SSPRK(3,2).

The TVD2 and TVD3 (total variation diminishing) schemes were also analysed with respect to their SSP (strong stability preserving) properties by Kraaijevanger [14]. Their coefficients were first derived by Heun [16] and Fehlberg [17] from a different viewpoint. They are the explicit Runge–Kutta schemes of second order with two stages (TVD2) and of third order with three stages (TVD3) which have the largest domain for which the SSP property holds among all schemes of such order and such number of stages, i.e. they are the optimum SSPRK(2,2) and SSPRK(3,3) schemes. The SSPRK(3,2) scheme is the optimum one among all three-stage explicit Runge–Kutta schemes with SSP property, if the approximate order is required to be only two instead of three (see Kraaijevanger [14] for proofs of these results). It can be implemented with the same memory consumption as TVD2 [18, 19]. The Butcher arrays [e.g., 14, 5] and the Shu–Osher arrays [7] of all mentioned schemes are given in Table 2 resp. Table 3.

We note that all schemes are explicit schemes. According to Wang and Spiteri [13], they are all linearly unstable in theory when coupled with the WENO5 scheme except TVD3. But the Courant numbers we use are small enough in terms of Motamed et al. [20] to make the combination with WENO5 stable in practical applications.

0	1	0	1/2	1/2	1/2
1	1	1/2	1	1/2	1/2
$A_{\text{TVD2}}$	1/2	1/2	$A_{\text{SSPRK}(3,2)}$	1/3	1/3
0	1	1	1/4	1/4	2/3
1	1	1	1/4	1/4	2/3
1/2	1/2	1/6	1/6	2/3	
$A_{\text{TVD3}}$	1/6	1/6	2/3		

Table 2: The Butcher arrays of the explicit schemes considered in this paper. From left to right: TVD2, SSPRK(3,2), TVD3.

## 2. Analytical Test Cases

In practice, the order of accuracy is not sufficient to describe the efficiency of a Runge–Kutta method. As described in Ap-

scheme	order	stages	$\alpha_i$			$\beta_i$		
Euler	1	1	1			1		
TVD2	2	2	1	1/2	1/2	0	1/2	
SSPRK(3,2)	2	3	1	0	1	0	1/2	
			1/3	0	2/3	0	0	1/3
TVD3	3	3	1	3/4	1/4	0	1/4	
			1/3	0	2/3	0	0	2/3

Table 3: The Shu–Osher arrays [7] of the explicit schemes considered in this paper.

pendix A.6 in LeVeque [5], we assume that the error  $\varepsilon$  of a method decays with the step size  $h$  as

$$\varepsilon(h) \approx Ch^p, \quad (15)$$

where  $p$  is the (*empirical*) *order of convergence* or *order of accuracy* and  $C$  is the *error constant* of the method.  $\varepsilon(h)$  is the numerical error at grid spacing  $h$ . A higher order method may, for a given grid, deliver worse results than a lower order scheme due to its high error constant  $C$  [p. 35, 21].

$p$  and  $C$  can be estimated from a numerical solution if the exact (or at least, very accurate) solution is known by comparing the error for several values of  $h$ . If, for example, the resolution is increased by a factor 2, the convergence rate  $p$  can be estimated by

$$p = \log_2(\varepsilon(h)/\varepsilon(h/2)). \quad (16)$$

Then, the error constant of the method can be calculated by

$$C = \varepsilon(h)/h^p. \quad (17)$$

The obtained values depend on the test problem and on the norm chosen to measure the error size.

We compare the efficiency and accuracy of several numerical schemes by solving the advection equation

$$\frac{\partial \phi}{\partial t} + u \frac{\partial \phi}{\partial x} = 0 \quad (18)$$

for  $t \in (0, 2]$  and  $x \in [0, 1]$  with periodic boundary conditions. The advection velocity  $u$  is set to 1. The analytical solution of the advection equation (18) at time  $t$  is  $\phi(x, t) = \phi(x - t, 0)$ . With the initial condition

$$\phi(x, 0) = 1 + 0.1 \sin(2\pi x), \quad (19)$$

the analytical solution stays smooth for all times. Therefore, this is an appropriate test case for determining the empirical order of accuracy and the error constants of a method.

Given discontinuous initial data,

$$\phi(x, 0) = \begin{cases} 1, & \text{if } 0.1 < x < 0.3, \\ 0, & \text{else,} \end{cases} \quad (20)$$

the convergence order is restricted by the smoothness of the solution. By comparing the numerical solution to the analytical one, we calculate the mean  $L^2$  error at  $t = 2$  s [cf. Appendix A.5 in 5] for a set of spatial and temporal resolutions.

For the advection equation, the (advective) Courant number  $\sigma$  is defined by

$$\sigma = |u| \frac{\delta t}{\delta x}. \quad (21)$$

Next, we solve the one-dimensional diffusion equation

$$\frac{\partial \phi}{\partial t} - D \frac{\partial^2 \phi}{\partial x^2} = 0 \quad (22)$$

for  $t \in (0, 50]$  and  $x \in [0, 1]$  with periodic boundary conditions and with initial data

$$\phi(x, 0) = 1.1 + 0.1 \sin(2\pi x). \quad (23)$$

The analytical solution is

$$\phi(x, t) = 1.1 + 0.1 \exp(-D\pi^2 t) \sin(2\pi x). \quad (24)$$

$D > 0$  is the (constant) diffusion coefficient which we choose as  $10^{-3}$ . For the diffusion equation, we define the (diffusive) Courant number  $\sigma$  by

$$\sigma = D \frac{\delta t}{\delta x^2}. \quad (25)$$

### 2.1. Errors of Runge–Kutta Schemes

For the following, we choose the fifth order WENO scheme to discretise the advection equation in space, and compare the efficiency of several Runge–Kutta schemes for the analytical test problems from Section 2. The results are given for the smooth initial condition (19) in Tables A.14, A.15, A.16 and A.17 for the Euler forward, the TVD2, the TVD3, and the SSPRK(3,2) scheme, respectively. For the discontinuous initial condition (20), they can be found in Tables B.18, B.19, B.20 and B.21. In each row, the spatial resolution is fixed, whereas in the columns, the temporal resolution is constant. Since  $\phi$  is of magnitude 1, the absolute errors shown are also relative errors.

For advective problems, we see the error for a fixed Courant number on the diagonal of each of the error tables. If the solution was not stable for the particular choice of spatial and temporal resolution, we do not give a number for the error size. In most cases, the algorithm is stable only if  $\sigma < 1$ .

From these data we can deduce the size of the temporal and spatial error for each scheme, and its dependence on the Courant number. For the smooth initial condition (19), we observe that the error  $\varepsilon(\delta x, \delta t)$  of the Euler scheme is never smaller than about  $10^{-4}$ . It shows approximately first order convergence in time. For many combinations of  $\delta t$  and  $\delta x$ , decreasing  $\delta x$  does not lead to a decrease in the error, since the error is dominated by the error of the time integration scheme. We conclude

that the Euler forward scheme is not efficient unless the spatial resolution is very coarse. Then, the maximum allowed Courant numbers are rather small.

For the other schemes, the error reaches much smaller magnitudes down to approximately machine precision. In most cases, temporal and spatial error are balanced or the spatial error dominates except for the regions where both resolutions are either very coarse or very fine. The TVD3 scheme shows the smallest errors, but these are only reached with very high spatial and temporal resolution.

For the discontinuous problem, the errors are much larger. For a large range of combinations of  $\delta t$  and  $\delta x$ , the error is nearly independent of the temporal scheme. It does decrease with spatial resolution, but at a much slower rate determined by the smoothness of the solution. Nevertheless, the stability properties are different. The Euler forward scheme is always unstable for  $\sigma \geq 1$ , except for very coarse resolution, and shows non-monotonic error convergence. All other schemes give stable solutions with  $\sigma = 1$ , but often they are very inaccurate.

In Figure 1, we show the error convergence of the numerical solution of the advection equation with smooth initial data (19) (top panel) and with discontinuous initial data (20) (middle panel) for the four Runge–Kutta scheme considered in this paper. We also show fits of the form (15) to the error convergence. The parameters  $C$  and  $p$  of the fits are given in Table 4 for the smooth case and in Table 5 for the discontinuous case. For a given set of pairs  $(h_i, \varepsilon_i)$ , the fitting parameters  $C$  and  $p$  as defined in equation (15) are obtained by solving the linear system

$$\begin{pmatrix} \log_{10} h_1 & 1 \\ \log_{10} h_2 & 1 \\ \vdots & \vdots \\ \log_{10} h_n & 1 \end{pmatrix} \begin{pmatrix} p \\ \log_{10} C \end{pmatrix} = \begin{pmatrix} \log_{10} \varepsilon_1 \\ \log_{10} \varepsilon_2 \\ \vdots \\ \log_{10} \varepsilon_n \end{pmatrix}. \quad (26)$$

In the smooth case, WENO5 with Euler forward time integration yields first order convergence, whereas the combination with TVD2 and SSPRK(3,2) converges with second order. On average, the error constant of SSPRK(3,2) is smaller than the one of TVD2. Using TVD3 as time integrator results in third order convergence.

For the discontinuous initial condition (20) the convergence order and the error constant for all integration schemes are very similar except for the Euler method. The accuracy of the numerical solution is limited by the smoothness of the analytical solution. Only the Euler forward method shows different convergence rates with much strongly varying error constants, indicating very irregular error convergence. The additional effort of using a three-stage scheme does not pay off in terms of accuracy compared to TVD2. In terms of stability, TVD2, TVD3 and SSPRK(3,2) are quite similar.

From Figure 1, we investigate the influence of the Courant number  $\sigma$  on the accuracy of the numerical solution. On the left panels,  $\sigma = 0.5$ , whereas on the right panels,  $\sigma = 0.25$ . In the smooth case, halving  $\sigma$  leads to a decrease in error size by a factor 4 for the two second-order schemes and a factor 8 for TVD3, whereas the changes are much smaller for the discontinuous problem. We conclude that the accuracy of the numerical

solution is in the smooth case limited by the time integration scheme for fine grid spacing and by the spatial discretisation for coarse grid spacing, but in the discontinuous problem by the spatial accuracy only (for those schemes which are actually stable).

For the diffusion test case (22) with the smooth initial condition (23), the errors of the numerical solutions calculated at  $t = 50$  s are shown in Tables C.22, C.23, C.24 and C.25. The error plots for fixed Courant numbers  $\sigma$  are shown in Figure 2 together with fits of the form (15). The parameters  $C$  and  $p$  of the fits are given in Table 6.

Keeping  $\sigma$  fixed and decreasing the grid spacing means decreasing the time step size quadratically. Therefore, the empirical convergence rates and error constants shown in Table 6 exhibit second to fourth order convergence since the convergence rate of the time integration is doubled. The overall convergence is then restricted by the fourth order spatial discretisation as defined in equations (7). The increase in error for very small grid spacings is due to rounding errors, and is larger the more stages the time integration scheme has.

From Table 10 in Kupka et al. [6] we deduce that the maximum Courant number  $\sigma$  as defined in equation (25) for diffusive terms is 0.375 for TVD2, 0.299 for TVD3 and 0.672 for SSPRK(3,2). This is confirmed by the stability behaviour of the numerical solution of the test problem (22) with initial condition (23). Only SSPRK(3,2) yields stable results with  $\sigma = 0.5$ . We conclude that the high maximum Courant number of SSPRK(3,2) makes it the most efficient scheme for diffusion-type equations even though its theoretical order of accuracy in time is only 2. We note that even with non-smooth initial data, the solution of the diffusion equation (22) is smooth for  $t > 0$  and the error sizes converge in the same manner [22].

One could argue that formally, it is inconsistent to measure convergence orders by using the spatial resolution  $\delta x$  as  $h$  in formula (15) since the number of degrees of freedom increases quadratically for the advection equation or even cubic for the diffusion equation due to the smaller time steps induced by the CFL condition. But from a practical point of view, modifying the spatial resolution and choosing a Courant number is the only way to control the accuracy of an existing simulation. Therefore, measuring the order of error decay when decreasing the spatial resolution while keeping the Courant number fixed gives the type of “convergence order” which is encountered in applications.

We note that the efficiency of the time integration scheme depends on the expected smoothness and the required accuracy of the numerical solution. Therefore, in the next section we try to estimate the typical accuracy and smoothness of a simulation of solar surface convection. But first, we compare the WENO spatial discretisation with other standard schemes for the case of the advection equation.

## 2.2. Errors of WENO Schemes compared to Standard Schemes

In this paragraph, we compare the computational efficiency of the WENO5 scheme and TVD2 time integration with two standard schemes: the first order accurate Upwind and the second order accurate Lax–Friedrichs scheme [23].

On a given (equidistant) grid, the one-dimensional conservation law

$$\frac{\partial \phi}{\partial t} + \frac{\partial F(\phi)}{\partial x} = 0 \quad (27)$$

with the analytical flux function  $F$  is discretised in space in a conservative fashion by [9]

$$\frac{\partial \phi_i}{\partial t} + \frac{H_{i+\frac{1}{2}} - H_{i-\frac{1}{2}}}{\delta x} = 0. \quad (28)$$

A numerical scheme defines how the numerical flux  $H_{i+\frac{1}{2}}$  is calculated. The procedure for the Upwind, the Lax–Friedrichs and WENO5 scheme is summarised in Algorithms 1, 2 and 3, respectively.

---

**Algorithm 1** Calculation of the numerical flux  $H_{i+\frac{1}{2}}$  with the first order Upwind method assuming  $\frac{\partial F}{\partial \phi} > 0$ .

---

$$1: H_{i+\frac{1}{2}} = F(\phi_i)$$


---

---

**Algorithm 2** Calculation of the numerical flux  $H_{i+\frac{1}{2}}$  with the second order Lax–Friedrichs method assuming  $\frac{\partial F}{\partial \phi} > 0$ .

---

$$1: H_{i+\frac{1}{2}} = 0.5 \cdot \left( (F(\phi_{i+1}) + F(\phi_i)) + \frac{\delta x}{\delta t} \cdot (\phi_i - \phi_{i+1}) \right)$$


---

It is obvious that the complexity of the WENO scheme is much larger than for the lower order schemes. For calculating the numerical flux function in one grid point, only one evaluation of the analytical flux function  $F$  is necessary for the upwind method. For the Lax–Friedrichs method, 2 evaluations of  $F$ , 3 additions and 2 multiplications are necessary. But for the WENO method, at least 5 evaluations of  $F$ , 25 additions, 28 multiplications, 4 divisions and 9 exponentiations are required (the latter can be expressed through 9 multiplications since they are just of power 2). However, given sufficient memory, i.e. if  $F(\phi_i)$  can be stored, the most expensive operation in non-academic examples, the computation of  $F(\phi_i)$  has to be done only once for each scheme which significantly reduces the costs of particularly WENO5 in such applications.

In Figure 3, the error convergence and fits of the form (15) of the numerical solution of the advection equation (18) with smooth initial data (19) and non-smooth initial data (20) obtained with the Upwind, the Lax–Friedrichs, and the WENO5 scheme combined with TVD2 time integration are shown. The parameters  $C$  and  $p$  of the fits are given in Table 7 for the smooth case and Table 8 for the discontinuous case.

From Figure 3 we deduce that the empirical order of accuracy of the WENO5 algorithm together with a second order time integration such as TVD2 [7] is two which is also obtained with the Lax–Friedrichs method (cf. Strikwerda [23]). Nevertheless, the error constant is much smaller than with the Lax–Friedrichs method. In the smooth case, we observe about a factor of 8 for  $\sigma = 0.25$ , whereas for  $\sigma = 0.125$ , it is about a factor of 12. Similar is true for the discontinuous test case. We conclude that the numerical error obtained with WENO5 and TVD2 can

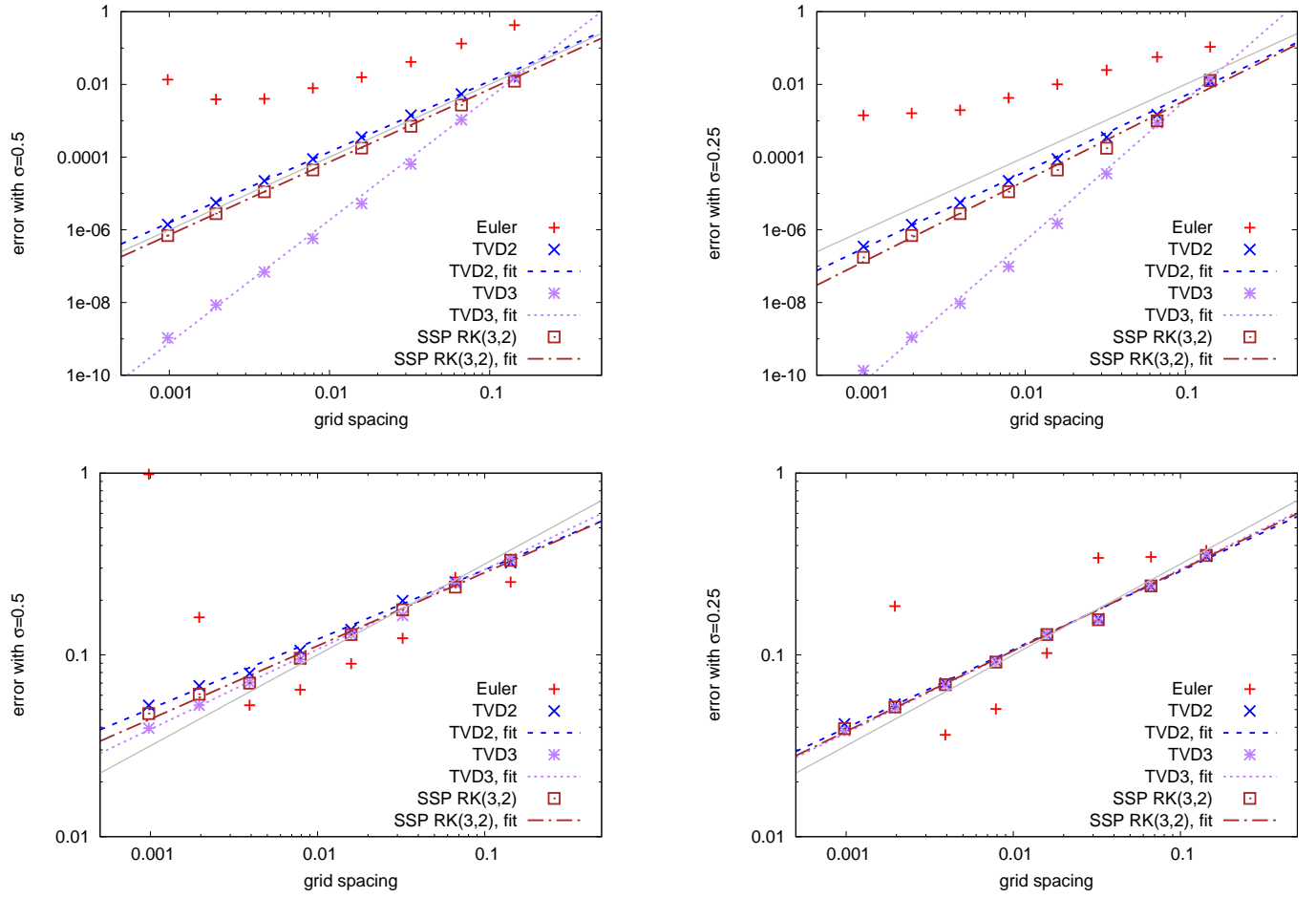


Figure 1: Comparison of error convergence fits and actual error data for  $\sigma = 0.5$  (left) and  $\sigma = 0.25$  (right). Spatial discretisation is done with the WENO5 scheme. Top panel: advection equation with smooth initial data (19). The grey line indicates second-order convergence. Bottom panel: advection equation with discontinuous initial data (20). The grey line indicates square-root convergence. Euler forward is unstable for small grid spacing for both Courant numbers and no fit is shown for this method as it would not apply to the whole range of grid spacings.

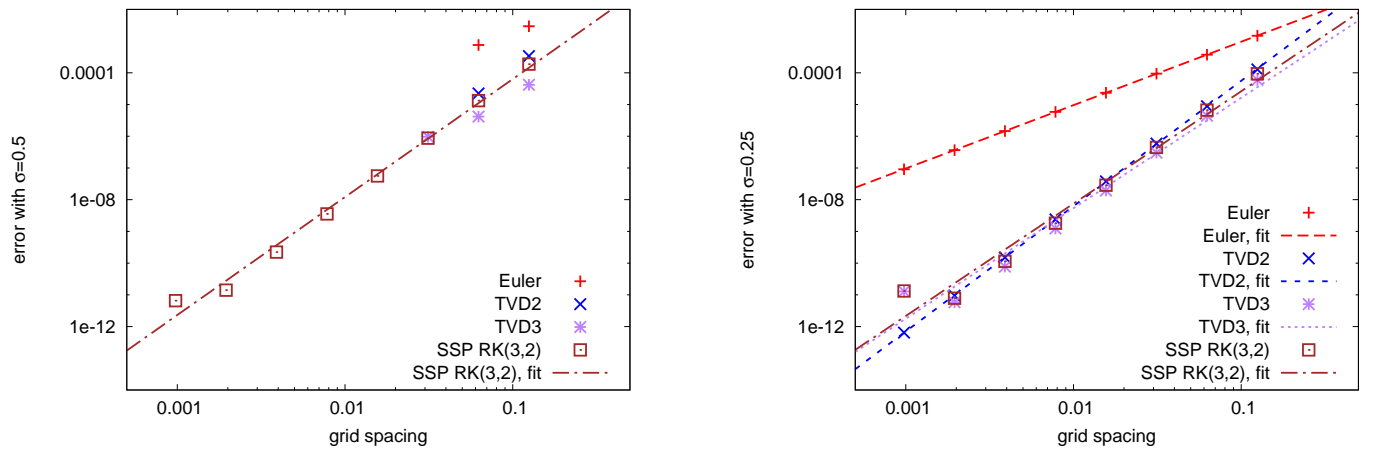


Figure 2: Comparison of error convergence fits and actual error data for  $\sigma = 0.5$  (left) and  $\sigma = 0.25$  (right) for the diffusion equation with smooth initial data (19).

scheme	$\sigma = 1.0$		$\sigma = 0.5$		$\sigma = 0.25$		$\sigma = 0.125$		$\sigma = 0.0625$	
	$p$	$C$	$p$	$C$	$p$	$C$	$p$	$C$	$p$	$C$
Euler							0.98	3.10e-1	0.83	7.88e-2
TVD2	0.90	2.97e-1	1.95	1.08e0	2.09	6.09e-1	2.34	6.35e-1	2.66	9.69e-1
TVD3	3.05	1.24e1	3.38	1.05e1	3.86	2.57e1	4.35	9.82e1	4.68	2.76e2
SSPRK(3,2)	1.11	1.62e-1	2.00	7.42e-1	2.21	5.84e-1	2.49	7.53e-1	2.83	1.36e0

Table 4: Empirical order of accuracy  $p$  and error constants  $C$  for WENO with several time integration schemes and fixed Courant numbers  $\sigma$  when solving (18) & (19).

scheme	$\sigma = 1.0$		$\sigma = 0.5$		$\sigma = 0.25$		$\sigma = 0.125$		$\sigma = 0.0625$	
	$p$	$C$	$p$	$C$	$p$	$C$	$p$	$C$	$p$	$C$
Euler							0.60	1.31e0	0.56	1.05e0
TVD2	0.30	8.63e-1	0.38	7.09e-1	0.43	7.79e-1	0.45	8.23e-1	0.45	8.23e-1
TVD3	0.27	6.41e-1	0.44	8.12e-1	0.45	8.35e-1	0.45	8.30e-1	0.45	8.24e-1
SSPRK(3,2)	0.37	7.51e-1	0.40	7.18e-1	0.44	8.14e-1	0.45	8.27e-1	0.45	8.24e-1

Table 5: Empirical order of accuracy  $p$  and error constants  $C$  for WENO with several time integration schemes and fixed Courant numbers  $\sigma$  when solving (18) & (20).

be controlled by adapting  $\sigma$ , whereas with the Lax–Friedrichs method, it is nearly independent of  $\sigma$ . The error of any first order method as, e.g., the upwind method (cf. again Strikwerda [23]), is larger by several magnitudes. A very high amount of grid points is required for them to reach an acceptable error size.

We measure the wall clock time of the simulations performed on an Intel Core2 Duo CPU with 3.0 GHz clock rate. By multiplying the error with the wall clock time of the simulation, we can compare the efficiency of the schemes considered in this section. For both the smooth and non-smooth case, we show the cost-weighted errors of the Upwind, the Lax–Friedrichs and the WENO5 scheme with TVD2 time integration in Figure 4. We choose  $\sigma = 0.0625$  since otherwise the wall clock times are too short to be reliable. In the smooth case, WENO5 is much more efficient over the whole range of resolutions considered in this test. The higher computational complexity of the scheme leads to a more than proportional increase in accuracy. For the discontinuous problem, the computational costs are slightly higher since the accuracy of the numerical solution is determined by the analytical smoothness of the solution. Nevertheless, the difference is small, and the higher complexity of WENO5 pays off in higher stability of the scheme (the difference is a factor of 3 to 4 for large grid spacing whereas it ranges from 8 to 30 comparing the WENO5 scheme with Lax–Friedrichs and even up to  $10^4$  when comparing WENO5 to the Upwind scheme). A much higher Courant number can be used for WENO5 and TVD2 without considerably increasing the error size, making the scheme much more efficient. For coarse grid spacing Lax–Friedrichs and the Upwind scheme are even unstable for the discontinuous solution or at best equally efficient as WENO5.

Another point which we did not mention so far are memory requirements: much more grid points are needed with lower order schemes to reach the accuracy of WENO5 which leads to a tremendous increase in memory consumption in particular in higher dimensions. We conclude that WENO5 schemes are not only more accurate than standard schemes, but also computationally more efficient.

From the comparisons done in Muthsam et al. [10] and in Muthsam et al. [1], it follows that WENO5 without artificial diffusivities yields also much more accurate results than other high-order methods considered in their work which, however, always require such stabilisations.

When applying the WENO method to systems of conservation laws, the state variables must be transformed into the eigenstate which increases the computation time. On the other hand, methods where no transformation is needed are less accurate and artificial diffusivities are necessary to stabilise the solution, e.g. around shock fronts, which at the bottom line is less efficient [10, 1].

In this section, we compared our methods to the most basic first and second order accurate schemes. For more rigorous comparisons concerning the spatial discretisation, we refer, e.g., to Shu [8]. In contrast, the purpose of these tests is to give orientation concerning the magnitude and behaviour of the spatial error whereas we focus on the error from the time integration and the interplay with diffusion terms.

### 3. Error Size in Simulations of Solar Surface Convection

To measure the typical error in simulations of solar surface convection with ANTARES, we performed two three-dimensional simulations which only differ in the numerical resolution. Their specifications are summarised in Table 9. The purpose of this section is to give an estimate of the typical error size of our numerical simulations in a realistic setting. This estimate will be used in Section 4 to compare the efficiency of several time integration schemes for this particular type of computational problem.

We remark that these simulations are Large Eddy Simulations (LES), i.e., they do not resolve all scales of motion. All motions with length scales smaller than the grid resolution are modelled by the Smagorinsky subgrid model and by the numerical viscosity of the numerical scheme. Therefore, the measurement of “the error” is not trivial. Changing the resolution will

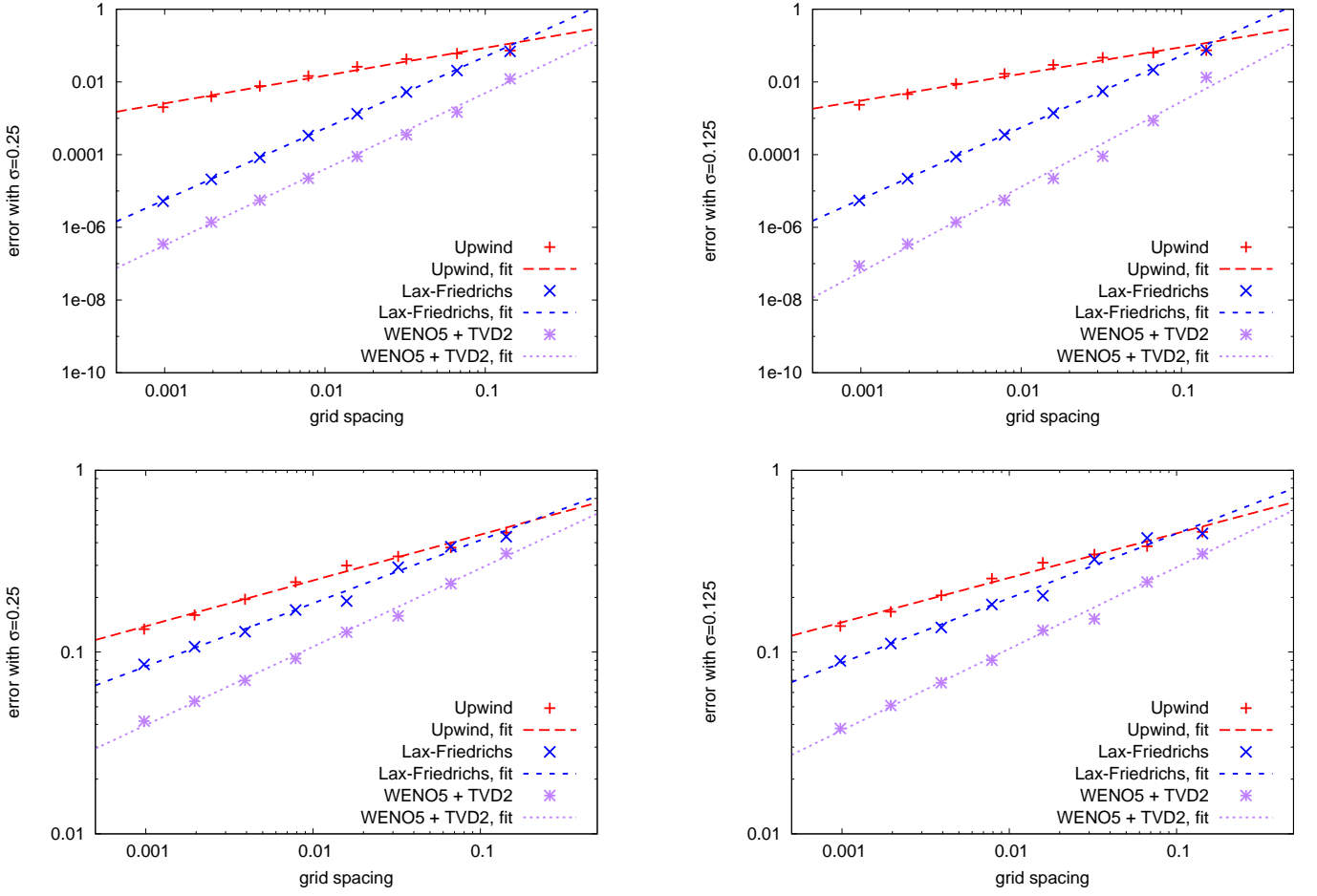


Figure 3: Comparison of error convergence fits and actual error data for  $\sigma = 0.25$  (left) and  $\sigma = 0.125$  (right) with the Upwind, the Lax–Friedrichs and the WENO5 scheme with TVD2 time integration. Top panel: advection equation with smooth initial data (19); bottom panel: advection equation with discontinuous initial data (20).

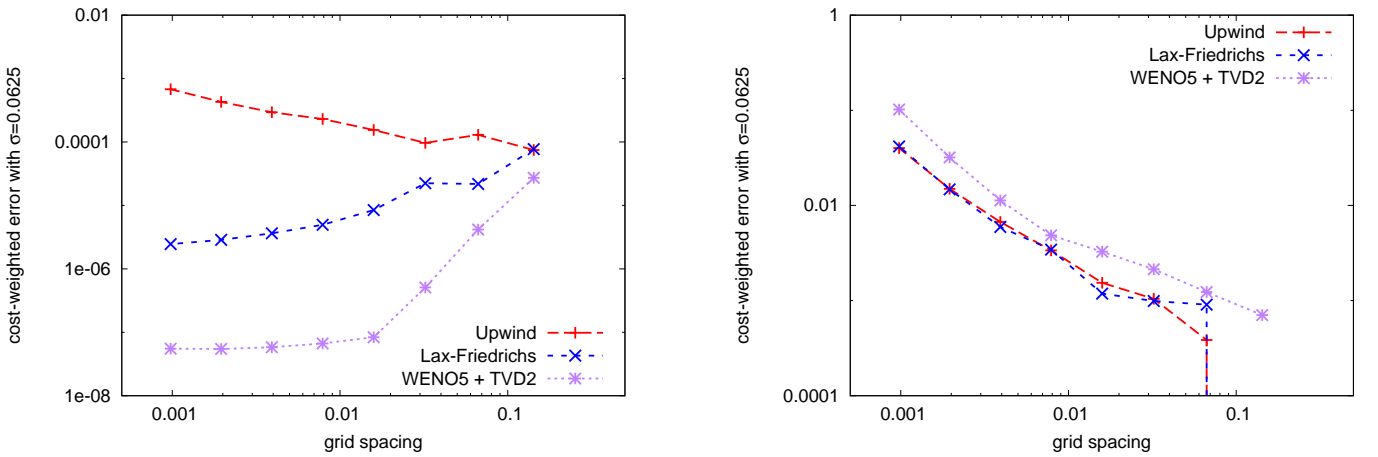


Figure 4: Cost-weighted error of the numerical solution of the advection equation (18) with smooth initial condition (19) and discontinuous initial condition (20) obtained with the Upwind, the Lax–Friedrichs and the WENO5 scheme combined with TVD2 time integration. Here,  $\sigma = 0.0625$ . The execution time of each simulation is measured with the `time` command and multiplied with the absolute error size. For the discontinuous problem, the cost-weighted error of WENO5 with TVD2 is slightly higher since the increase in computation time is not compensated by the decrease in error. For the smooth case, however, the cost-weighted error is much smaller. Furthermore, WENO5 with TVD2 gives accurate results even at much higher Courant numbers.



scheme	$\sigma = 0.5$		$\sigma = 0.25$		$\sigma = 0.125$		$\sigma = 0.0625$	
	$p$	$C$	$p$	$C$	$p$	$C$	$p$	$C$
Euler			2.00	9.49e-2	1.99	4.53e-2	1.98	2.08e-2
TVD2			3.95	5.00e-1	3.91	2.73e-1	3.91	2.31e-1
TVD3			3.48	4.95e-2	3.38	3.51e-2	3.25	2.31e-2
SSPRK(3,2)	3.72	3.34e-1	3.54	9.12e-2	3.39	4.08e-2	3.24	2.29e-2

Table 6: Empirical order of accuracy  $p$  and error constants  $C$  for WENO with several time integration schemes and fixed Courant numbers  $\sigma$  when solving (22) & (23).

---

**Algorithm 3** Calculation of the numerical flux  $H_{i+\frac{1}{2}}$  with WENO5 assuming  $\frac{\partial F}{\partial \phi} > 0$  [8].

---

1:

$$\begin{aligned}\beta_0 &= \frac{13}{12} \cdot (F(\phi_i) - 2 \cdot F(\phi_{i+1}) + F(\phi_{i+2}))^2 + \frac{1}{4} \cdot (3 \cdot F(\phi_i) - 4 \cdot F(\phi_{i+1}) + F(\phi_{i+2}))^2, \\ \beta_1 &= \frac{13}{12} \cdot (F(\phi_{i-1}) - 2 \cdot F(\phi_i) + F(\phi_{i+1}))^2 + \frac{1}{4} \cdot (F(\phi_{i-1}) - F(\phi_{i+1}))^2, \\ \beta_2 &= \frac{13}{12} \cdot (F(\phi_{i-2}) - 2 \cdot F(\phi_{i-1}) + F(\phi_i))^2 + \frac{1}{4} \cdot (F(\phi_{i-2}) - 4 \cdot F(\phi_{i-1}) + 3 \cdot F(\phi_i))^2\end{aligned}$$

2:

$$\tilde{\omega}_0 = \frac{0.3}{(\epsilon + \beta_0)^2}, \quad \tilde{\omega}_1 = \frac{0.6}{(\epsilon + \beta_1)^2}, \quad \tilde{\omega}_2 = \frac{0.1}{(\epsilon + \beta_2)^2}$$

3:

$$\omega_0 = \frac{\tilde{\omega}_0}{\tilde{\omega}_0 + \tilde{\omega}_1 + \tilde{\omega}_2}, \quad \omega_1 = \frac{\tilde{\omega}_1}{\tilde{\omega}_0 + \tilde{\omega}_1 + \tilde{\omega}_2}, \quad \omega_2 = \frac{\tilde{\omega}_2}{\tilde{\omega}_0 + \tilde{\omega}_1 + \tilde{\omega}_2}$$

4:

$$\begin{aligned}H_{i+\frac{1}{2}} &= \omega_0 \cdot \left( \frac{1}{3} \cdot F(\phi_i) + \frac{5}{6} \cdot F(\phi_{i+1}) - \frac{1}{6} \cdot F(\phi_{i+2}) \right) \\ &\quad + \omega_1 \cdot \left( -\frac{1}{6} \cdot F(\phi_{i-1}) + \frac{5}{6} \cdot F(\phi_i) + \frac{1}{3} \cdot F(\phi_{i+1}) \right) \\ &\quad + \omega_2 \cdot \left( \frac{1}{3} \cdot F(\phi_{i-2}) - \frac{7}{6} \cdot F(\phi_{i-1}) + \frac{11}{6} \cdot F(\phi_i) \right)\end{aligned}$$


---

change the results and convergence of the solution with grid spacing cannot be expected due to the chaotic nature of turbulence.

As an approximate estimate of the error size, we calculate the difference between the solutions on the finer and the coarser grid by point-wise comparison of the values on coinciding grid points, as described in Appendix A.6 in LeVeque [5]. The resulting error estimates in several variables and several norms are shown in Table 10.

We show the error right after the interpolation, after  $\sim 160$  s and after 950 s of simulation time. After the interpolation, the error is very small, but already after 160 s it has grown considerably. After 950 s, the two models have completely diverged, and we observe that the  $L^\infty$  error is much larger than the  $L^1$  and  $L^2$  error. This stems from the fact that near the optical surface, the motion of the fluid is turbulent, and changes in the numerical parameters as grid resolution produces arbitrarily large differences. Here, the pointwise changes due to increased reso-

lution are large compared to the rest of the simulation, and, as indicated by the huge numbers, can have completely diverged in the course of the simulation.

Therefore, we refrain from measuring the error pointwisely. Instead, we suggest to use the mean temperature profile for error measurement. In Figure 5 we observe that the mean temperature is much more stable, but still sensitive enough to changes in the resolution. The standard deviation of the temperature profile is even more sensitive, but since it approaches 0 it is not suited for calculating relative errors. Furthermore, its behaviour near the top boundary is strongly influenced by the boundary conditions [25]. The typical mean error of the temperature profile, i.e. the relative error in the  $L^1$  norm, is around 0.1 % to 0.5 %.

Of course, these numbers are only rough estimates. The influence of uncertainties in the solution of the radiative transfer equation, the equation of state, and the boundary conditions, to name only a few factors, is huge and difficult to number. Never-

scheme	$\sigma = 0.5$		$\sigma = 0.25$		$\sigma = 0.125$		$\sigma = 0.0625$	
	$p$	$C$	$p$	$C$	$p$	$C$	$p$	$C$
Upwind	0.83	4.95e-1	0.76	5.01e-1	0.74	4.92e-1	0.72	4.86e-1
Lax–Friedrichs	1.97	3.69e0	1.97	4.62e0	1.97	4.97e0	1.98	5.07e0

Table 7: Empirical order of accuracy  $p$  and error constants  $C$  for the Upwind and the Lax–Friedrichs scheme with fixed Courant numbers when solving (18) & (19).

scheme	$\sigma = 0.5$		$\sigma = 0.25$		$\sigma = 0.125$		$\sigma = 0.0625$	
	$p$	$C$	$p$	$C$	$p$	$C$	$p$	$C$
Upwind	0.24	6.81e-1	0.25	7.90e-1	0.24	7.91e-1	0.24	7.86e-1
Lax–Friedrichs	0.33	7.79e-1	0.35	9.18e-1	0.36	1.02e0	0.37	1.11e0

Table 8: Empirical order of accuracy  $p$  and error constants  $C$  for the Upwind and the Lax–Friedrichs scheme with fixed Courant numbers when solving (18) & (20).

	resolution [km]	grid points	box size [Mm]	binning
Model 1	$19.5 \times 40.0^2$	$195 \times 150^2$	$3.8 \times 6.0^2$	non-grey
Model 2	$9.74 \times 20.0^2$	$389 \times 300^2$	$3.8 \times 6.0^2$	non-grey

Table 9: Basic parameters of the two three-dimensional models from Section 3. Model 2 was started from Model 1. The data were mapped to the finer grid by interpolation, and both models were run for 950 s. Both models use the Smagorinsky subgrid model [24] to represent motions with scales smaller than the grid resolution, and a Gauss–Radau rule with 18 rays for the angular integration in the radiative transfer solver. They use the open boundary conditions BC 3b from Grimm–Strele et al. [25] at the bottom, the LLNL equation of state [26], the non-grey opacities from Kurucz [27, 28], the opacity data from Iglesias and Rogers [29] for the deep interior, and the composition from Grevesse and Noels [30]. The WENO5 scheme was used for spatial discretisation, and SSPRK(3,2) for time integration.

theless, our tests indicate the magnitude of the error which is far from the asymptotic regime where we can profit from the fast error convergence of higher order time integration schemes.

In hydrodynamical simulations of similar grid size, but without the extra uncertainties introduced by radiative transfer and where all scales of motion are resolved on the grid scale (i.e., DNS), the magnitude of the error is typically of the size 0.1 % when the simulation is about to become turbulent (cf. Fig. 12 to 15 in Kupka et al. [6] and Fig. 7 in Happenhofer et al. [11]).

Finally, we want to determine the area ratio of smooth to non-smooth regions. For this purpose, we calculate the nonlinearity index NI as defined in equation (8) of Taylor et al. [31]. Therein, the nonlinear weights  $\omega_j$  of the interpolating polynomials in the WENO reconstruction scheme as described in Algorithm 3 are compared to the optimal linear weights  $d_j$ . In smooth regions, they should be of the same size, whereas in non-smooth regions the weight of one of the parabolae should be much higher. Then, the nonlinearity index NI defined by

$$NI = \frac{1}{\sqrt{k(k+1)}} \left( \sum_{j=0}^k \left( 1 - \frac{(k+1)\omega_j/d_j}{\sum_{l=0}^k \omega_l/d_l} \right)^2 \right)^{\frac{1}{2}}, \quad (29)$$

will be close to 1. Here,  $k$  is the width of the stencil of each interpolation polynomial such that the order of the reconstruction process is  $2k - 1$ . For the fifth order variant summarised in Algorithm 3,  $k = 3$ .

We plot NI as calculated in the WENO reconstruction procedure in the first characteristic variable for reconstruction in the

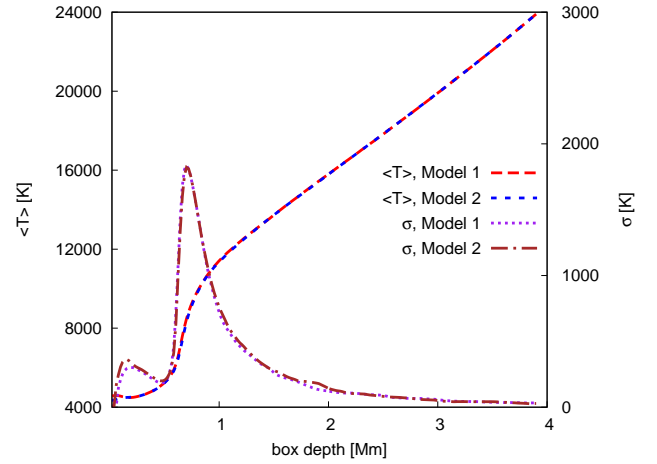


Figure 5: Mean temperature profile and standard deviation of Models 1 and 2 as described in Table 9. Horizontal averages are calculated after  $\sim 950$  s of simulation time.

vertical ( $x$ ) direction for one snapshot of Model 1. In Figure 6, we show NI together with the entropy at a fixed geometrical depth near the optical surface. Actually, NI is located at the half-integer node, but we ignore this small visualisation error. In Figure 7, the mean value, the standard deviation, the minimum and the maximum error in each vertical layer is plotted.

We conclude that NI captures the dynamics of surface convection very well. In regions where the flow is turbulent — mainly the intergranular lanes near the optical surface (which is located at a geometrical depth of around 800 km) —, its value is large whereas it is reasonably small in smooth regions of the flow. We remark that the size of the minimum value of NI depends on the design of the nonlinear weights in the WENO reconstruction [31]. In our tests,  $\epsilon$  as defined in Algorithm 3 is fixed to  $10^{-40}$ .

We conclude that even though NI is a purely numerical parameter, it also has a physical meaning and is a good indicator of whether a solution is smooth or not. Counting the number of points where  $NI < 0.25$  and where  $NI > 0.5$ , we get a good estimate of the area ratio of smooth to non-smooth regions. In this particular simulation, the fraction of non-smooth regions never exceeds 8 % except for the uppermost layers which are strongly influenced by the boundary conditions. Over the whole simula-

variable	unit	type	$t = 0$ s			$t = 160$ s			$t = 950$ s		
			$L^1$	$L^2$	$L^\infty$	$L^1$	$L^2$	$L^\infty$	$L^1$	$L^2$	$L^\infty$
$\rho$	$\text{g cm}^{-3}$	absolute	1.40e-12	3.74e-11	5.13e-8	1.39e-8	2.77e-8	9.56e-7	3.64e-8	6.14e-8	9.81e-7
$T$	K	absolute	0.0	0.0	16.3	60.8	179.3	4067.6	242.5	624.3	4971.6
$\rho$		relative	0.0 %	0.1 %	4.6 %	2.5 %	5.6 %	80.3 %	6.6 %	18.1 %	641.4 %
$T$		relative	0.0 %	0.0 %	0.1 %	0.7 %	2.0 %	60.1 %	2.7 %	7.6 %	86.2 %
$\langle T \rangle$	K	absolute	0.0	0.0	0.0	14.9	31.2	127.8	22.8	47.3	228.9
$\langle T \rangle$		relative	0.0 %	0.0 %	0.0 %	0.2 %	0.4 %	1.7 %	0.3 %	0.8 %	5.0 %

Table 10: The error sizes in density  $\rho$  and temperature  $T$  calculated by point-wisely comparing the simulations described in Table 9 according to the procedure from LeVeque [5] right after the interpolation and for two snapshots taken after 160 s and  $\sim 950$  s of simulation time. Both models originally coincided on the grid points of Model 1. The norms are calculated as described in the cited reference. The relative errors are calculated by dividing the absolute difference by the value of Model 1.  $\langle \cdot \rangle$  stands for horizontal averaging.

tion box, we can estimate the ratio to be

$$\frac{\text{volume where the flow is non-smooth}}{\text{volume where the flow is smooth}} \approx 0.05. \quad (30)$$

Therefore, even though the fraction of non-smooth regions is not negligible, the flow in the simulation box is mostly smooth.

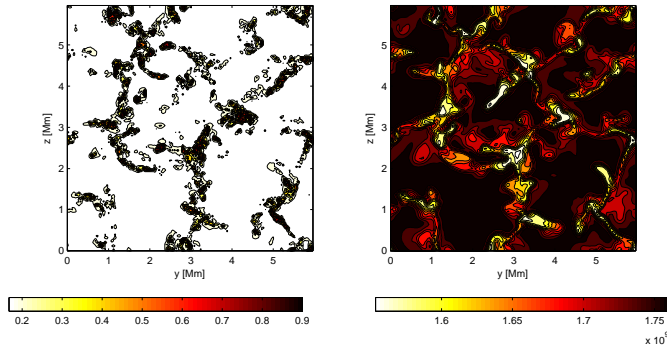


Figure 6: Left: snapshot of the nonlinearity index NI; right: the entropy of the three-dimensional model, both at a geometrical depth of around 1 Mm. The optical surface is at a geometrical depth of around 800 km. We observe that NI is largest in the intergranular lanes where the fluid motion is most turbulent [32, 33]. On top of each granule, the flow is rather smooth such that NI is small.

#### 4. Calculation of Computational Costs

In this section, we want to estimate and compare the computational costs of simulations of solar surface convection with the WENO5 scheme for spatial discretisation and the four Runge–Kutta schemes described in Section 1 for time integration, and under the conditions described in Section 3. We leave the spatial discretisation and the problem setup unchanged and investigate the influence of the time integration scheme only on the accuracy and computational costs of such a simulation.

The reason to use higher-order time integration schemes is that we expect more accurate results with less computation time than with the first-order Euler method. Clearly, all of the higher order schemes from Section 1 fulfil this for all grid resolutions and for both the advection and the diffusion equation.

It is more difficult to say which one of the three higher order methods is the best for our specific purposes. Since the time

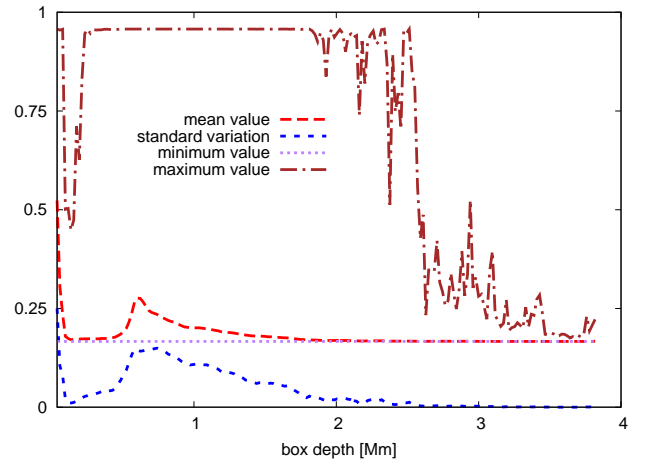


Figure 7: Mean value, standard deviation, minimum and maximum of the nonlinearity index NI at a specific vertical depth. We observe that NI reaches both its maximum values and its maximum average just below the optical surface. Deeper in the convection zone, the flow is smoother but NI never falls below a value of around 0.17.

step size is determined via the conditions (21) or (25) once the grid spacing is set, the grid spacing  $h$  and the Courant number  $\sigma$  are the only degrees of freedom to control the accuracy of the numerical solution. We formulate

**Problem 1.** *Given a relative accuracy  $\varepsilon_{\text{rel}}$  and a Courant number  $\sigma$ , which grid spacing is necessary for a computational cube of side length  $L$ , and how many time steps are needed for a time interval of length  $T$ ?*

Given a relative accuracy  $\varepsilon_{\text{rel}}$  and a Courant number  $\sigma$ , we can calculate the required relative grid spacing  $h$  to reach this accuracy by interpolating in the tables given in Appendix A, Appendix B or Appendix C, depending on whether the problem is advective or diffusive and whether the solution is smooth or non-smooth. The grid spacing  $\delta x$  of the simulation can be calculated via  $h = \delta x/L$ , where  $h$  is the (relative) grid spacing obtained using the table interpolation. Note that  $h$  is dimensionless.

In three dimensions, we need  $N_h = h^{-3}$  grid points for a cube with side length  $L$ . For an advection equation with advection

velocity  $u$ ,

$$N_t = n_{\text{stages}} \frac{T}{\delta t} \text{ with } \delta t = \frac{\sigma \delta x}{|u|} \quad (31)$$

integration steps are needed to cover a time interval of length  $T$ . The number of stages of the Runge–Kutta method is  $n_{\text{stages}}$ , and  $\sigma$  is the Courant number. The quantity  $\alpha := |u|T/L$  is a dimensionless quantity depending on the problem. Therefore, we define

$$N_t^* := N_t / \alpha = \frac{n_{\text{stages}}}{\sigma h}. \quad (32)$$

Then, the computational costs  $\gamma$  corresponding to the number of evaluations of the differential operator are given by

$$\gamma = N_h \cdot N_t = N_h \cdot N_t^* \cdot \alpha, \quad (33)$$

or scaled by the problem-dependent factor  $\alpha$ ,

$$\gamma^* = \gamma / \alpha. \quad (34)$$

For a diffusion equation,

$$N_t = n_{\text{stages}} \frac{T}{\delta t} \text{ with } \delta t = \frac{\sigma \delta x^2}{D}. \quad (35)$$

Similarly,  $\beta := DT/L^2$  is dimensionless and problem-dependent, and we define the scaled number of time steps  $N_t^*$  by

$$N_t^* := N_t / \beta = \frac{n_{\text{stages}}}{\sigma h^2} \quad (36)$$

and the scaled computational costs  $\gamma^*$  by

$$\gamma^* = \gamma / \beta. \quad (37)$$

In Table 11, the scaled computational costs with each scheme are calculated for an advective problem with smooth initial condition, corresponding to the data from Appendix A. According to the data from Table 10, we choose a relative accuracy of  $5 \cdot 10^{-3}$ . The Euler forward scheme is by far the most expensive one. It needs a relative grid spacing smaller than 0.01 to reach this error size. For the higher-order schemes, much larger grid spacings can be chosen.

We observe that for TVD3 and SSPRK(3,2), increasing  $\sigma$  from 0.25 to 0.5 leads to only a slightly smaller required relative grid spacing  $h$ . The computational costs are considerably decreased. Therefore, the Courant number should be set as large as the stability of the method allows it. Consequently, SSPRK(3,2) and TVD3 are the most efficient schemes since they allow Courant numbers of 0.5, as indicated by the data in Tables A.17 and A.16 and confirmed by numerical experiments with solar surface convection simulations. TVD2 is most efficient when comparing all schemes with fixed Courant number of 0.25, but it is not stable with higher Courant numbers. The differences in efficiency of TVD3 and SSPRK(3,2) are negligible.

With discontinuous initial data (20), the error size is much larger. Using a relative error size of  $2.5 \cdot 10^{-1}$  results in scaled computational costs as summarised in Table 12.

We deduce from Table 12, that again, Euler forward is very inefficient, whereas for all higher-order schemes, the required grid spacing is of similar orders of magnitude. Since the error is dominated by the spatial one and the smoothness of the solution, increasing the Courant number does not considerably decrease the accuracy. Once more, SSPRK(3,2) with  $\sigma = 0.5$  turns out to be more efficient than TVD2 with  $\sigma = 0.25$ .

In contrast to the advection equation where stability limits for  $\sigma$  must be found by experiment, there are analytical methods to determine the maximum admissible Courant number for each time integration scheme. From Table 10 in Kupka et al. [6] we deduce that the maximum Courant number  $\sigma$  as defined in equation (25) for diffusive terms is 0.187 for Euler forward, 0.375 for TVD2, 0.299 for TVD3 and 0.672 for SSPRK(3,2). For testing the efficiency of the diffusion equation, we use the maximum allowed Courant numbers from Kupka et al. [6] for each scheme multiplied by 3/4 due to the stability constraint given in equation (48) in Happenhofer et al. [11]. For the diffusion equation, we expect much smaller errors due to the smoothing properties of the diffusion equation. Therefore, we calculate the computational costs for a relative accuracy of  $1.0 \cdot 10^{-6}$ .

scheme	Euler	TVD2	TVD3	SSPRK(3,2)
$\sigma$	0.187	0.375	0.299	0.672
$\varepsilon_{\text{rel}}$	$1.0 \cdot 10^{-6}$			
$h$	4.19e-3	3.24e-2	3.65e-2	3.15e-2
$N_h$	1.36e7	2.95e4	2.06e4	3.19e4
$N_t^*$	4.06e5	6.79e3	1.00e4	5.98e3
$\gamma^*$	5.52e12	2.00e8	2.07e8	1.91e8

Table 13: Computational costs for diffusive problem with smooth initial condition.

The computational costs of the Euler forward scheme exceed the costs of the higher order schemes by several magnitudes. The costs with SSPRK(3,2) are significantly smaller than with TVD2 and TVD3, even though the advantage is smaller than one would expect from the difference in maximum allowed Courant numbers.

In conclusion, for both advection and diffusion equations the WENO5 and the fourth order conservative finite difference scheme described in Happenhofer et al. [11], applied to the advection and diffusion operator, respectively, combined with SSPRK(3,2) time integration are more efficient and more accurate than combinations with any other time integration schemes tested, both for smooth and non-smooth flows. We benefit from the high stability of SSPRK(3,2) and from the fact that *on grid sizes affordable in practice*, the spatial error usually is much larger than the temporal one. This justifies the additional efforts required for the implementation of SSPRK(3,2), even though its theoretical order of accuracy is lower than TVD3 and it has more stages than TVD2.

Changes of the time-integration scheme do not affect the number of grid cell updates per CPU second performed by the code, but they do change the overall number of updates needed

scheme	Euler	TVD2	TVD3		SSPRK(3,2)	
$\sigma$	0.25	0.25	0.25	0.5	0.25	0.5
$\varepsilon_{\text{rel}}$	$5 \cdot 10^{-3}$					
$h$	8.84e-3	8.32e-2	8.24e-2	7.97e-2	8.37e-2	7.75e-2
$N_h$	1.45e6	1.74e3	1.79e3	1.98e3	1.70e3	2.15e3
$N_t^*$	4.53e2	9.62e1	1.46e2	7.53e1	1.43e2	7.74e1
$\gamma^*$	6.56e8	1.67e5	2.61e5	1.49e5	2.44e5	1.66e5

Table 11: Computational costs for advective problem with smooth initial condition.

scheme	Euler	TVD2	TVD3		SSPRK(3,2)	
$\sigma$	0.25	0.25	0.25	0.5	0.25	0.5
$\varepsilon_{\text{rel}}$	$2.5 \cdot 10^{-1}$					
$h$	1.41e-2	6.94e-2	6.68e-2	6.44e-2	6.83e-2	7.17e-2
$N_h$	3.58e5	2.99e3	3.35e3	3.75e3	3.14e3	2.71e3
$N_t^*$	2.84e2	1.15e2	1.80e2	9.32e1	1.76e2	8.37e1
$\gamma^*$	1.02e8	3.45e5	6.02e5	3.49e5	5.52e5	2.27e5

Table 12: Computational costs for advective problem with non-smooth initial condition.

for the simulation of a fixed time span. From Tables 11 and 13 we conclude that the achievable change of required grid cell updates is of the order of several tens of percent. This number directly translates into a speedup in terms of computational time, if the spatial discretisation is not changed.

We emphasize that these results do not tell that lower order schemes are *in general* more efficient than higher order schemes. In fact, our analysis only applied to simulations of solar surface convection with the specific numerical schemes we used. In particular, there might be other Runge–Kutta schemes (as, e.g., the ones presented in Ketcheson [18]) which are even more efficient. Nevertheless, our analysis provides a valuable tool to assess the achievable efficiency with a certain combination of numerical schemes and for a specific application.

## Acknowledgements

We acknowledge financial support from the Austrian Science fund (FWF), projects P25229 and P21742. HGS wants to thank the MPA Garching for a grant for a research stay in Garching. Calculations have been performed at the VSC clusters of the Vienna universities.

## Appendix A. Error Sizes for the Advection Equation with Smooth Initial Data

## Appendix B. Error Sizes for the Advection Equation with Discontinuous Initial Data

## Appendix C. Error Sizes for the Diffusion Equation with Smooth Initial Data

## References

- [1] H. J. Muthsam, F. Kupka, B. Löw-Baselli, C. Obertscheider, M. Langer, P. Lenz, *NewA* 15 (2010) 460 – 475.

- [2] E. Mundprecht, H. J. Muthsam, F. Kupka, *MNRAS* 435 (2013) 3191 – 3205.
- [3] F. Zaussinger, H. Spruit, *A&A* 554 (2013) A119.
- [4] E. F. Toro, *Riemann solvers and numerical methods for fluid dynamics: a practical introduction*, Springer Berlin New–York Heidelberg, 2009.
- [5] R. J. LeVeque, *Finite Difference Methods for Ordinary and Partial Differential Equations. Steady State and Time Dependent Problems*, Society for Industrial and Applied Mathematics (SIAM), 2007.
- [6] F. Kupka, N. Happenhofer, I. Higuera, O. Koch, *JCP* 231 (2012) 3561 – 3586.
- [7] C.-W. Shu, S. Osher, *JCP* 77 (1988) 439 – 471.
- [8] C.-W. Shu, *International Journal of Computational Fluid Dynamics* 17 (2003) 107 – 118.
- [9] B. Merriman, *Journal Of Scientific Computing* 19 (2003) 309 – 322.
- [10] H. J. Muthsam, B. Löw-Baselli, C. Obertscheider, M. Langer, P. Lenz, F. Kupka, *MNRAS* 380 (2007) 1335 – 1340.
- [11] N. Happenhofer, H. Grimm-Strele, F. Kupka, B. Löw-Baselli, H. J. Muthsam, *JCP* 236 (2013) 96 – 118.
- [12] S. Gottlieb, C.-W. Shu, E. Tadmor, *SIAM Review* 43 (2001) 89 – 112.
- [13] R. Wang, R. J. Spiteri, *SIAM J. Numer. Anal.* 45 (2007) 1871 – 1901.
- [14] J. F. B. M. Kraaijevanger, *BIT* 31 (1991) 482 – 528.
- [15] D. I. Ketcheson, C. B. Macdonald, S. Gottlieb, *Applied Numerical Mathematics* 59 (2009) 373 – 392.
- [16] K. Heun, *Z. Math. Phys* 45 (1900) 23 – 38.
- [17] E. Fehlberg, *Computing* 6 (1970) 61 – 71.
- [18] D. I. Ketcheson, *SIAM J. Sci. Comput.* 30 (2008) 2113–2136.
- [19] N. Happenhofer, O. Koch, F. Kupka, *ASC Report 27*, Institute for Analysis and Scientific Computing, Vienna UT, 2011.
- [20] M. Motamed, C. B. Macdonald, S. J. Ruuth, *Journal Of Scientific Computing* 47 (2011) 127 – 149.
- [21] J. H. Ferziger, M. Perić, *Computational Methods for Fluid Dynamics*, 3rd ed., Springer, Berlin, 2002.
- [22] L. C. Evans, *Partial Differential Equations*, volume 19 of *Graduate Studies in Mathematics*, 2nd ed., American Mathematical Society, 2002.
- [23] J. C. Strikwerda, *Finite Difference Schemes and Partial Differential Equations*, Wadsworth & Brooks/Cole, 1989.
- [24] J. Smagorinsky, *MWR* 91 (1963) 99 – 164.
- [25] H. Grimm-Strele, F. Kupka, B. Löw-Baselli, E. Mundprecht, F. Zaussinger, P. Schiansky, *NewA* 34 (2015) 278 – 293.
- [26] F. J. Rogers, F. J. Swenson, C. A. Iglesias, *ApJ* 456 (1996) 902.
- [27] R. Kurucz, *Kurucz CD-ROM No. 13*. Cambridge, Mass.: Smithsonian Astrophysical Observatory (1993).
- [28] R. Kurucz, *Kurucz CD-ROM No. 2*. Cambridge, Mass.: Smithsonian

$\delta x \setminus \delta t$	0.1250	0.0625	0.0312	0.0156	0.0078	0.0039	0.0020	0.0010	0.0005	0.0002	0.0001
0.1250		4.26e-1	1.07e-1	3.39e-2	9.93e-3	7.07e-3	1.00e-2	1.18e-2	1.27e-2	1.32e-2	1.34e-2
0.0625			1.33e-1	5.66e-2	2.37e-2	1.06e-2	4.74e-3	2.01e-3	7.66e-4	4.62e-4	5.96e-4
0.0312				4.14e-2	2.48e-2	1.15e-2	5.55e-3	2.71e-3	1.33e-3	6.46e-4	3.09e-4
0.0156					1.57e-2	1.00e-2	5.62e-3	2.76e-3	1.36e-3	6.79e-4	3.38e-4
0.0078						7.87e-3	4.24e-3	2.77e-3	1.37e-3	6.82e-4	3.40e-4
0.0039							4.01e-3	1.95e-3	1.39e-3	6.84e-4	3.41e-4
0.0020								3.87e-3	1.60e-3	5.94e-4	3.41e-4
0.0010									1.36e-2	1.41e-3	3.87e-4

Table A.14:  $\varepsilon(\delta x, \delta t)$  for the combination of WENO5 with Euler forward when solving (18) & (19).

$\delta x \setminus \delta t$	0.1250	0.0625	0.0312	0.0156	0.0078	0.0039	0.0020	0.0010	0.0005	0.0002	0.0001
0.1250	7.68e-2	1.53e-2	1.21e-2	1.33e-2	1.36e-2	1.36e-2	1.37e-2	1.37e-2	1.37e-2	1.37e-2	1.37e-2
0.0625		2.21e-2	5.39e-3	1.47e-3	8.55e-4	8.35e-4	8.40e-4	8.43e-4	8.43e-4	8.43e-4	8.43e-4
0.0312			6.10e-3	1.41e-3	3.50e-4	9.03e-5	3.64e-5	3.10e-5	3.09e-5	3.10e-5	3.10e-5
0.0156				6.78e-3	3.55e-4	8.86e-5	2.21e-5	5.58e-6	1.65e-6	1.01e-6	9.65e-7
0.0078					4.28e-3	8.90e-5	2.22e-5	5.56e-6	1.39e-6	3.48e-7	9.12e-8
0.0039						2.26e-3	2.23e-5	5.57e-6	1.39e-6	3.48e-7	8.69e-8
0.0020							1.09e-3	5.57e-6	1.39e-6	3.48e-7	8.70e-8
0.0010								5.86e-4	1.39e-6	3.48e-7	8.71e-8

Table A.15:  $\varepsilon(\delta x, \delta t)$  for the combination of WENO5 with TVD2 when solving (18) & (19).

- Astrophysical Observatory (1993).
- [29] C. A. Iglesias, F. J. Rogers, ApJ 464 (1996) 943.
- [30] N. Grevesse, A. Noels, in: N. Prantzos, E. Vangioni-Flam, M. Casse (Eds.), Origin and Evolution of the Elements, 1993, pp. 15 – 25.
- [31] E. M. Taylor, M. Wu, M. P. Martin, JCP 223 (2007) 384 – 397.
- [32] R. F. Stein, A. Nordlund, Solar Physics 192 (2000) 91 – 108.
- [33] F. Kupka, Turbulent Convection and Simulations in Astrophysics, Springer Lecture Notes in Physics 756, 2009, pp. 49–105.

$\delta x \setminus \delta t$	0.1250	0.0625	0.0312	0.0156	0.0078	0.0039	0.0020	0.0010	0.0005	0.0002	0.0001
0.1250	2.19e-2	1.54e-2	1.38e-2	1.38e-2	1.37e-2	1.37e-2	1.37e-2	1.37e-2	1.37e-2	1.37e-2	1.37e-2
0.0625		2.89e-3	1.06e-3	8.75e-4	8.49e-4	8.45e-4	8.43e-4	8.44e-4	8.43e-4	8.43e-4	8.43e-4
0.0312			3.07e-4	6.38e-5	3.49e-5	3.14e-5	3.11e-5	3.10e-5	3.10e-5	3.10e-5	3.10e-5
0.0156				3.59e-5	5.29e-6	1.49e-6	1.03e-6	9.73e-7	9.66e-7	9.65e-7	9.65e-7
0.0078					4.41e-6	5.76e-7	9.77e-8	3.83e-8	3.09e-8	3.00e-8	2.99e-8
0.0039						5.48e-7	6.93e-8	9.46e-9	1.99e-9	1.06e-9	9.44e-10
0.0020							6.85e-8	8.58e-9	1.10e-9	1.62e-10	4.56e-11
0.0010								8.55e-9	1.07e-9	1.34e-10	1.76e-11

Table A.16:  $\varepsilon(\delta x, \delta t)$  for the combination of WENO5 with TVD3 when solving (18) & (19).

$\delta x \setminus \delta t$	0.1250	0.0625	0.0312	0.0156	0.0078	0.0039	0.0020	0.0010	0.0005	0.0002	0.0001
0.1250	3.55e-2	1.23e-2	1.28e-2	1.36e-2	1.37e-2	1.37e-2	1.37e-2	1.37e-2	1.37e-2	1.37e-2	1.37e-2
0.0625	1.58e-1	1.14e-2	2.71e-3	9.91e-4	8.34e-4	8.39e-4	8.42e-4	8.43e-4	8.43e-4	8.43e-4	8.43e-4
0.0312		9.20e-2	2.86e-3	7.05e-4	1.76e-4	5.14e-5	3.20e-5	3.09e-5	3.09e-5	3.10e-5	3.10e-5
0.0156				7.14e-4	1.78e-4	4.43e-5	1.11e-5	2.89e-6	1.16e-6	9.73e-7	9.64e-7
0.0078				8.09e-2	1.79e-4	4.45e-5	1.11e-5	2.78e-6	6.94e-7	1.76e-7	5.22e-8
0.0039						4.06e-4	1.11e-5	2.78e-6	6.96e-7	1.74e-7	4.35e-8
0.0020							2.49e-4	2.79e-6	6.96e-7	1.74e-7	4.35e-8
0.0010								1.55e-4	6.97e-7	1.74e-7	4.35e-8

Table A.17:  $\varepsilon(\delta x, \delta t)$  for the combination of WENO5 with SSPRK(3,2) when solving (18) & (19).

$\delta x \setminus \delta t$	0.1250	0.0625	0.0312	0.0156	0.0078	0.0039	0.0020	0.0010	0.0005	0.0002	0.0001
0.1250		2.52e-1	3.75e-1	3.38e-1	3.45e-1	3.53e-1	3.53e-1	3.55e-1	3.56e-1	3.56e-1	3.56e-1
0.0625		2.05e-3	2.67e-1	3.46e-1	2.32e-1	2.27e-1	2.38e-1	2.42e-1	2.46e-1	2.47e-1	2.48e-1
0.0312				1.24e-1	3.41e-1	2.25e-1	1.54e-1	1.40e-1	1.44e-1	1.48e-1	1.50e-1
0.0156					8.94e-2	1.02e-1	1.13e-1	9.45e-2	1.05e-1	1.12e-1	1.17e-1
0.0078						6.43e-2	5.04e-2	5.79e-2	6.61e-2	7.39e-2	8.05e-2
0.0039							5.28e-2	3.63e-2	4.09e-2	4.68e-2	5.23e-2
0.0020								1.61e-1	1.85e-1	2.89e-2	3.30e-2
0.0010									9.86e-1		2.26e-2

Table B.18:  $\varepsilon(\delta x, \delta t)$  for the combination of WENO5 with Euler forward when solving (18) & (20).

$\delta x \setminus \delta t$	0.1250	0.0625	0.0312	0.0156	0.0078	0.0039	0.0020	0.0010	0.0005	0.0002	0.0001
0.1250	4.64e-1	3.22e-1	3.49e-1	3.47e-1	3.52e-1	3.56e-1	3.55e-1	3.56e-1	3.56e-1	3.56e-1	3.56e-1
0.0625		3.67e-1	2.52e-1	2.38e-1	2.43e-1	2.46e-1	2.49e-1	2.48e-1	2.49e-1	2.49e-1	2.49e-1
0.0312			3.13e-1	1.99e-1	1.58e-1	1.52e-1	1.52e-1	1.52e-1	1.52e-1	1.52e-1	1.52e-1
0.0156				2.48e-1	1.38e-1	1.29e-1	1.32e-1	1.21e-1	1.21e-1	1.21e-1	1.21e-1
0.0078					1.93e-1	1.06e-1	9.20e-2	9.02e-2	9.00e-2	9.00e-2	9.00e-2
0.0039						1.58e-1	7.92e-2	6.98e-2	6.77e-2	6.76e-2	6.76e-2
0.0020							1.30e-1	6.75e-2	5.36e-2	5.08e-2	5.07e-2
0.0010								1.09e-1	5.27e-2	4.17e-2	3.80e-2

Table B.19:  $\varepsilon(\delta x, \delta t)$  for the combination of WENO5 with TVD2 when solving (18) & (20).

$\delta x \setminus \delta t$	0.1250	0.0625	0.0312	0.0156	0.0078	0.0039	0.0020	0.0010	0.0005	0.0002	0.0001
0.1250	3.66e-1	3.38e-1	3.56e-1	3.49e-1	3.53e-1	3.56e-1	3.55e-1	3.56e-1	3.56e-1	3.56e-1	3.56e-1
0.0625		3.28e-1	2.47e-1	2.42e-1	2.45e-1	2.47e-1	2.49e-1	2.48e-1	2.49e-1	2.49e-1	2.49e-1
0.0312			2.47e-1	1.65e-1	1.55e-1	1.52e-1	1.52e-1	1.52e-1	1.52e-1	1.52e-1	1.52e-1
0.0156				1.92e-1	1.30e-1	1.30e-1	1.32e-1	1.21e-1	1.21e-1	1.21e-1	1.21e-1
0.0078					1.74e-1	9.46e-2	9.11e-2	9.03e-2	9.00e-2	9.00e-2	9.00e-2
0.0039						1.48e-1	7.06e-2	6.83e-2	6.78e-2	6.76e-2	6.76e-2
0.0020							1.20e-1	5.29e-2	5.11e-2	5.08e-2	5.07e-2
0.0010								1.01e-1	3.96e-2	3.82e-2	3.80e-2

Table B.20:  $\varepsilon(\delta x, \delta t)$  for the combination of WENO5 with TVD3 when solving (18) & (20).

$\delta x \setminus \delta t$	0.1250	0.0625	0.0312	0.0156	0.0078	0.0039	0.0020	0.0010	0.0005	0.0002	0.0001
0.1250	3.49e-1	3.31e-1	3.53e-1	3.48e-1	3.52e-1	3.56e-1	3.55e-1	3.56e-1	3.56e-1	3.56e-1	3.56e-1
0.0625	4.48e-1	3.01e-1	2.36e-1	2.40e-1	2.44e-1	2.46e-1	2.49e-1	2.48e-1	2.49e-1	2.49e-1	2.49e-1
0.0312			1.99e-1	1.77e-1	1.56e-1	1.52e-1	1.52e-1	1.52e-1	1.52e-1	1.52e-1	1.52e-1
0.0156				1.54e-1	1.29e-1	1.29e-1	1.32e-1	1.21e-1	1.21e-1	1.21e-1	1.21e-1
0.0078					1.18e-1	9.58e-2	9.13e-2	9.02e-2	9.00e-2	9.00e-2	9.00e-2
0.0039						9.33e-2	6.99e-2	6.86e-2	6.77e-2	6.76e-2	6.76e-2
0.0020							7.42e-2	6.08e-2	5.17e-2	5.08e-2	5.07e-2
0.0010								6.28e-2	4.75e-2	3.93e-2	3.79e-2

Table B.21:  $\varepsilon(\delta x, \delta t)$  for the combination of WENO5 with SSPRK(3,2) when solving (18) & (20).

$\delta x \setminus \delta t$	1.95312	0.48828	0.24414	0.12207	0.06104	0.03052	0.01526	0.00763	0.00191	0.00048	0.00012
0.12500	6.92e-4	1.25e-4	3.14e-5	1.54e-5	3.88e-5	5.06e-5	5.64e-5	5.93e-5	6.15e-5	6.21e-5	6.22e-5
0.06250	7.56e-4	1.85e-4	9.03e-5	4.28e-5	1.91e-5	7.29e-6	1.37e-6	1.58e-6	3.80e-6	4.36e-6	4.50e-6
0.03125			9.42e-5	4.69e-5	2.33e-5	1.15e-5	5.60e-6	2.65e-6	4.34e-7	1.19e-7	2.57e-7
0.01562					2.35e-5	1.17e-5	5.86e-6	2.92e-6	7.15e-7	1.64e-7	2.64e-8
0.00781							5.86e-6	2.93e-6	7.31e-7	1.82e-7	4.45e-8
0.00391									7.31e-7	1.83e-7	4.56e-8
0.00195										1.83e-7	4.57e-8
0.00098											4.56e-8

Table C.22:  $\varepsilon(\delta x, \delta t)$  for the combination of WENO5 with Euler forward when solving (22) & (23).

$\delta x \setminus \delta t$	1.95312	0.48828	0.24414	0.12207	0.06104	0.03052	0.01526	0.00763	0.00191	0.00048	0.00012
0.12500	7.74e-5	6.30e-5	6.25e-5	6.23e-5	6.22e-5	6.23e-5	6.23e-5	6.23e-5	6.23e-5	6.23e-5	6.23e-5
0.06250	2.24e-5	5.61e-6	4.81e-6	4.61e-6	4.56e-6	4.55e-6	4.54e-6	4.54e-6	4.54e-6	4.54e-6	4.54e-6
0.03125			5.90e-7	3.74e-7	3.21e-7	3.08e-7	3.04e-7	3.03e-7	3.03e-7	3.03e-7	3.03e-7
0.01562					3.78e-8	2.41e-8	2.06e-8	1.98e-8	1.95e-8	1.95e-8	1.95e-8
0.00781							2.39e-9	1.52e-9	1.25e-9	1.24e-9	1.24e-9
0.00391									9.59e-11	8.01e-11	7.78e-11
0.00195										6.80e-12	4.81e-12
0.00098											5.06e-13

Table C.23:  $\varepsilon(\delta x, \delta t)$  for the combination of WENO5 with TVD2 when solving (22) & (23).



$\delta x \setminus \delta t$	1.95312	0.48828	0.24414	0.12207	0.06104	0.03052	0.01526	0.00763	0.00191	0.00048	0.00012
0.12500	6.15e-5	6.21e-5	6.22e-5	6.22e-5	6.22e-5	6.22e-5	6.23e-5	6.23e-5	6.23e-5	6.23e-5	6.23e-5
0.06250	4.18e-6	4.52e-6	4.54e-6	4.54e-6	4.54e-6	4.54e-6	4.54e-6	4.54e-6	4.54e-6	4.54e-6	4.54e-6
0.03125		9.61e-7	3.02e-7	3.03e-7	3.03e-7	3.03e-7	3.03e-7	3.03e-7	3.03e-7	3.03e-7	3.03e-7
0.01562					1.95e-8	1.95e-8	1.95e-8	1.95e-8	1.95e-8	1.95e-8	1.95e-8
0.00781							1.23e-9	1.24e-9	1.24e-9	1.24e-9	1.24e-9
0.00391									7.77e-11	7.79e-11	8.17e-11
0.00195										8.04e-12	2.58e-11
0.00098											2.56e-11

Table C.24:  $\varepsilon(\delta x, \delta t)$  for the combination of WENO5 with TVD3 when solving (22) & (23).

$\delta x \setminus \delta t$	1.95312	0.48828	0.24414	0.12207	0.06104	0.03052	0.01526	0.00763	0.00191	0.00048	0.00012
0.12500	6.95e-5	6.25e-5	6.23e-5	6.23e-5	6.22e-5	6.23e-5	6.23e-5	6.23e-5	6.23e-5	6.23e-5	6.23e-5
0.06250	1.33e-5	5.06e-6	4.68e-6	4.57e-6	4.55e-6	4.54e-6	4.54e-6	4.54e-6	4.54e-6	4.54e-6	4.54e-6
0.03125		8.74e-7	4.46e-7	3.39e-7	3.12e-7	3.05e-7	3.04e-7	3.03e-7	3.03e-7	3.03e-7	3.03e-7
0.01562				5.61e-8	2.86e-8	2.18e-8	2.01e-8	1.96e-8	1.95e-8	1.95e-8	1.95e-8
0.00781						3.55e-9	1.81e-9	1.38e-9	1.24e-9	1.24e-9	1.24e-9
0.00391								2.23e-10	8.68e-11	7.86e-11	8.26e-11
0.00195									1.41e-11	8.65e-12	2.84e-11
0.00098										6.55e-12	2.73e-11

Table C.25:  $\varepsilon(\delta x, \delta t)$  for the combination of WENO5 with SSPRK(3,2) when solving (22) & (23).